Research papers

A method for the lifetime sensorless estimation of surface and core temperature in lithium-ion batteries via online updating of electrical parameters

Pablo Rodríguez-Iturriaga [a,*], David Anseán [b], Juan Antonio López-Villanueva [a], Manuela González [b], Salvador Rodríguez-Bolívar [a]

[a] Department of Electronics and Computer Technology, Faculty of Sciences, Granada, 18071, Andalusia, Spain
[b] Department of Electrical Engineering, Polytechnic School of Engineering, Gijon, 33204, Asturias, Spain

ARTICLE INFO

ABSTRACT

Online temperature estimates are essential to the thermal monitoring and control of battery cells for battery management systems (BMSs). Due to hardware limitations, there has been a surge in interest in sensorless approaches for both surface and core temperatures. On this account, several methods have been proposed in the literature for the coestimation of state of charge (SOC) and temperature via RC-based electrical and thermal models and Extended Kalman Filters (EKFs). However, the stability and reliability of these schemes over the complete cell lifetime, when the effects of battery aging become apparent, have not been addressed thoroughly. In this article, a dual state-parameter estimation is carried out on an enhanced equivalent circuit model to coestimate the SOC and SOH on a commercial nickel-rich, silicon–graphite cell throughout its entire lifetime. A thermal model has been characterized based on the previous electrical model for the estimation of surface and core temperature of the cell. The continuous updating and correction of electrical parameters prove to be critical for temperature estimations to remain accurate in the long run, yielding a root mean square error (RMSE) in surface temperature below 1.2 °C for as long as 800 cycles.

1. Introduction

Lithium-ion batteries (LIBs) currently power most electronic devices, and are a key enabling technology in applications ranging from renewable energies to electric vehicles [1,2]. Aiming to increase the performance of LIBs, several approaches are currently ongoing, with the introduction of silicon into the anodic materials being one of the most promising innovations [3]. State-of-the-art commercial 18650 batteries containing a blend of silicon and graphite (Si–Gr) in the negative electrode and a mixture of nickel-rich materials (i.e., NMC811, NCA) on the positive electrode may increase the energy density by 25% when compared to standard 18650 cells without silicon [4–7]. Thanks to this remarkable energy density improvement, Si–Gr batteries are expected to be deployed in consumer electronics and next-generation electric vehicles (EVs) [8–10]. As with the introduction of any novel battery technology, several questions remain unresolved in cell chemistries containing silicon regarding battery performance and reliability over prolonged operation cycling [11–13], which make estimations of the long-term behavior of cells with battery technology even more challenging [14].

On the other hand, temperature is one of the main factors that influence the safety and performance of LIBs [15], as well as their rate of degradation and remaining useful life (RUL) [16]. The increasing prevalence of LIBs in EVs has led to a greater need for faster charging and discharging schemes, which can cause cell temperatures to rise considerably [17]. Consequently, the thermal monitoring of lithium-ion cells, especially in larger battery packs, is an essential function of a battery management system (BMS). However, physically measuring the surface temperature of individual cells would entail a substantial instrumentation cost, as well as additional difficulties with hardware and wiring [18]. For this reason, several procedures have been proposed in order to determine the temperature of battery cells without the need for a dedicated sensor. Plenty of these methods are based on information extracted from Electrochemical Impedance Spectroscopy (EIS) tests. McCarthy et al. [19] presented a comprehensive review on the applications of EIS measurements, including internal temperature estimations. This was recognized as a promising line of research since the need for physical sensors is no longer present and temperature estimations may be acquired faster than with existing methods [20].

Nevertheless, some inconsistencies were pointed out in [19] regarding what features should be searched for and at which frequencies or frequency range, as well as the method to establish the correlation between the identified features and the estimated internal temperature.

Conversely, the core and surface temperatures of a cell may also be approximated without sensors by means of thermal modeling and the estimation of the heat generation rate from current and voltage measurements. Several control-oriented thermal models for cylindrical lithium ion batteries were presented in [21], which range from lumped to PDE-based thermal models, and it was concluded that a 2RC equivalent circuit model constitutes a reasonable compromise between accuracy and computational cost. An alternative to thermal RC-networks is obtained by reducing the 1-D heat equation to a system of ordinary differential equations (ODEs) in order to achieve a state-space representation that retains a physical description of the process. However, the applicability of these procedures throughout the lifetime of the cell is commonly not considered; as a result, their accuracy is not guaranteed in the long term if the heat generation term is not updated accordingly. As a matter of fact, Ludwig et al. [22] recently demonstrated that degradation and the resistance growth associated with aging greatly affect the accuracy of temperature estimations, and improved their previous pulse-based sensorless method [23] by compensating these effects with offset correction and accurate state of charge (SOC) estimations. Nonetheless, this empirical method requires precise SOC and capacity measurements, as well as *a priori* knowledge of the long-term behavior of the battery cell, which may hinder its online application. This proves that, if the temperature is estimated via thermal modeling, a battery model that is able to account for capacity loss as well as the change in electrical parameters that affect the heat generation rate is essential to the long-term accuracy and reliability of the temperature estimations.

Electrical battery models can be broadly divided into three categories [24,25]: electrochemical models, semi-empirical models and data-driven approaches. As computational burden remains a limiting factor in online monitoring algorithms, semi-empirical models, and in particular equivalent circuit models (ECMs) are notably widespread. In addition, ECMs are practical in BMSs due to the simplicity of their implementation and their reduced computational requirements [26]. Still, standard ECMs present shortcomings regarding the reproduction of nonlinear behavior of LIBs as well as with their validation under broad operating conditions and degradation stages [27]. To circumvent these issues, there has been a recent surge in interest in extended, physics-informed ECMs that account for electrochemical processes such as solid-phase diffusion [28], nonlinear capacity effects [29], charge transfer processes [26,30] and double-layer capacitance at the electrode–electrolyte interface via fractional-order elements [31–33]. On the other hand, extended Kalman filters (EKFs) remain the most popular alternative for online estimation and monitoring [34]. Given the aforementioned issues, simultaneous parameter identification via Recursive Least Squares (RLS) algorithms [35–37], as well as state-parameter estimations via joint extended Kalman Filters [38], adaptive extended Kalman Filters [39] and dual-extended Kalman filters (DEKFs) [40–42] have been employed for continuous parameter updating. This way, long-term parameter variations due to the effects of cell degradation, which may be too complex to be included in a simple ECM, are estimated.

Nevertheless, making use of a DEKF in order to estimate cell capacity as a model parameter poses serious stability concerns after several cycles, as shown in [41]. This is due to the fact that battery degradation is a much slower process than voltage dynamics, so updating cell capacity every iteration of the algorithm introduces extraneous noise in the system that deteriorates both state and parameter estimations [43], compromising overall filter stability. For the reasons above, it becomes clear that a different approach is needed in order to estimate battery remaining capacity. Several empirical degradation models have been proposed [44–46], although they are chemistry dependent and not suitable for online estimation. For this purpose, straightforward capacity estimates as a direct measurement of the quotient $\Delta Q/\Delta SOC$ have also been presented [47], although this method requires extremely accurate SOC estimations. In order to reduce the influence of noisy measurements, RLS algorithms are often employed. A forgetting factor [48] may easily be added into the algorithm with the purpose of increasing the weight of recent measurements, so that capacity estimations reflect actual cell degradation in long-term operation.

In this article, we carry out a dual state-parameter estimation on an improved, physics-informed equivalent circuit model for the sensorless estimation of surface and core temperature on a commercial NMC811/Si–Gr cell throughout its cycle life. Dual state-parameter estimation for the electrical model [36,37], along with online capacity estimation, constitute an interesting alternative for updating electrical parameters and improving SOC estimations for long-term operation. For this purpose, both electrical and thermal models have been parameterized, and the performance of the proposed method is validated with experimental data of 800 cycles with a 2C discharge followed by a C/2 charge, which allow for a considerable temperature increment as well as a characterization of full the transient response of the thermal model. Our results show that this method enables the thermal model to remain valid in the long run, permitting the accurate estimation of the temperature increment in individual cells for their thermal monitoring and management. To the best of our knowledge, this is the first work that presents an online method for the estimation of the cell surface and core temperature throughout its lifetime with a restrained computational cost.

Consequently, this paper is organized as follows: the specification of the investigated cell, the experimental setup and the conducted tests are described in Section 2. The equivalent circuit model as well as the procedure to carry out dual state-parameter estimation are introduced in Section 3. In Section 4, the algorithm for SOH estimation is presented along with guidelines on when it should be employed. A two-state thermal model based on the proposed equivalent circuit model is characterized and analyzed in Section 5, while simulation results and comparisons between estimations and measurements are shown in Section 6. Finally, some concluding remarks are provided in the last section.

2. Experimental

For this study, commercial INR18650-35E cells from Samsung-SDI were acquired from an online vendor. According to the manufacturer, these cells exhibit a standard discharge capacity greater or equal than 3.4 Ah when discharged at 1C within the voltage limits (4.2 V charge, 2.65 V cut-off). The tests were carried out on a multichannel, high-precision series Arbin LBT20084 battery system with 24-bit and 18-bit resolution for voltage and current measurements, respectively. A Memmert environmental chamber was used to maintain the tested cell at a constant ambient temperature of 23 °C. The temperatures in both the climate chamber and the cell case were measured with T-type copper–constantan thermocouples with a standard tolerance of 1 °C and logged into the Arbin system. A general perspective of the battery tester along with the associated climatic chamber is shown in Fig. 1-(a), whereas a detail of the analyzed cell with its corresponding thermocouple and battery holder may be observed in Fig. 1-(b).

The testing strategy comprises four blocks (I–IV) [49], each block providing specific experimental results on the tested cell. In Block I, testing equipment preparation and accuracy verification is carried out. In Block II, the tested cell quality is evaluated. Block III comprises the Reference Performance Tests (RPTs), carried out to determine the thermodynamic, electrical and thermal characteristics of the cell under test. Block IV is the repetitive duty cycle scheme, and consisted of a series of continuous full charge and discharge cycles. The charging was performed at a constant current (CC) stage at C/2 (1.7 A) until

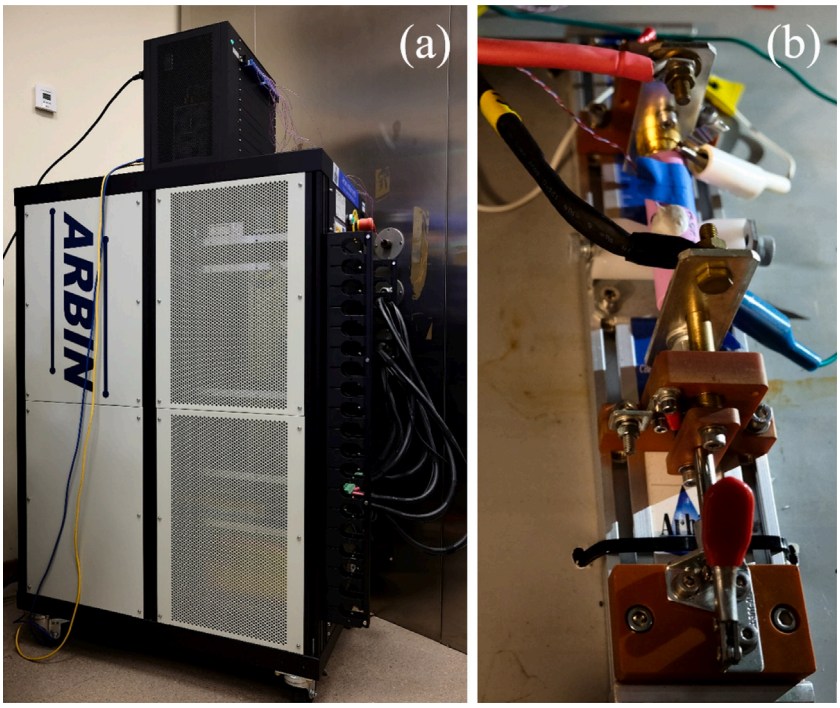

Fig. 1. (a) Arbin LBT20084 battery system and environmental chamber (b) Cell under test in the Arbin battery holder inside the climatic chamber, with its thermocouple attached with adhesive putty.

the cell reaches 4.2 V, followed by a constant voltage (CV) stage until the current declines to C/50 (68 mA). The discharge was carried out at 2C (6.8 A) CC until the 2.65 V cut-off voltage was reached. This charge/discharge sequence was performed continuously for 100 cycles, after which the RPTs (i.e., Block II) were performed again. The testing sequence (i.e., Block II and III) was repeated until the cell reached the end-of-cycling at 800 cycles. At that point, a final RPT was carried out and the cell testing was terminated. Due to the importance of the RPT scheme (i.e., Block III) to develop battery models and the identification of cell parameters, a more detailed description of the RPTs is provided below.

The RPTs quantitatively assess battery performance using standard testing equipment, providing as much information as possible without being intrusive. To develop the physics-informed equivalent circuit model presented in this work, three key testing schemes are performed during the RPTs, namely, (i) Thermodynamic testing, (ii) Internal resistance testing and (iii) Thermal testing. All testing was performed within the cell voltage limits (i.e., 4.2 V to 2.65 V).

1. Thermodynamic testing includes a set of two stabilization cycles at C/2 CC-CV charge and C/5 CC discharge, followed by the thermodynamic cycling with two cycles at C/25 CC, and a final C/50 CC cycle sampled at 1 mV. The thermodynamic cycling also comprises a two-hour rest-period between charge and discharge. This set of testing allows for the determination of the pseudo-OCV curve to decipher the OCV-SOC relationship.
2. Internal resistance testing includes a set of two stabilization cycles C/2 CC-CV charge and C/5 CC discharge, followed by a specific set of dynamic pulses. This methodology exhibits the electrochemical processes involved in a cell, deriving the contributions from the ohmic, charge transfer and polarization resistance [50–52]. The dynamic pulses were carried out at the following SOCs: 5%, 20%, 50%, 80% and 95%, both in charge and discharge. The peak pulse was rated to ±C/2 with a duration of 120 s, and a sampling rate of 0.5 mV or 1 ms (whichever is first) to acquire all representative data to construct the model. The current and voltage profiles of this testing scheme are shown in Fig. 2.
3. Thermal testing consists of six high-rate discharge cycles followed by a resting period to determine the thermal properties of the cell. The test consists of a C/2 CC-CV charge, followed by a maximum discharge rate at 2C CC and a temperature relaxation period of 2-hour rest. The data sampling rate is set to 1 s.

3. SOC estimation

As presented in Section 1, SOC estimation algorithms require an electrical model that is able to reproduce voltage dynamics as a function of a current input. Equivalent circuit models are widely employed in such algorithms due to their reduced computational cost and simple implementation. Nevertheless, they provide little insight into the actual electrochemical behavior and their parameters should either include SOC and temperature dependencies or be updated continuously for the model to be applicable in a wide range of operating conditions. Dual state-parameter estimation allows accounting for these dependencies as well as parameter variation and drift that occur in long-term operation.

3.1. Equivalent circuit model

Farmann et al. [26] presented seven equivalent circuit models to reproduce dynamic battery behavior, ranging from simplest to most complex. The equivalent circuit model used in this study is model 4 of said work (shown in Fig. 3), which is the most comprehensive model (including the current dependence of the charge-transfer resistance) that does not contain fractional-order elements, whose analysis and time-domain implementation is beyond the scope of this paper.

This model differs from a standard 3RC ECM in the fact that it accounts for the current dependence of the charge transfer resistance: the RC-element comprised of R_{ct} and C_1 with the fastest time constant τ_1 is responsible for capturing charge transfer processes occurring at the electrode–electrolyte interface [53]. The charge-transfer overpotential (η) is determined by the Butler–Volmer equation:

$$i = i_0 \left(\exp\left((1-\alpha)\frac{F\eta}{R_g T} \right) - \exp\left(-\alpha \frac{F\eta}{R_g T} \right) \right), \quad (1)$$

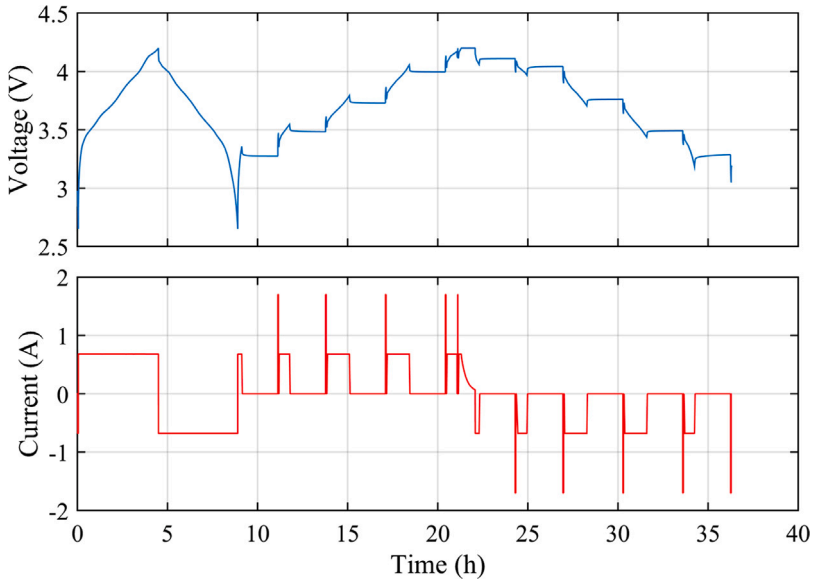

Fig. 2. Current and voltage profiles for the internal resistance test.

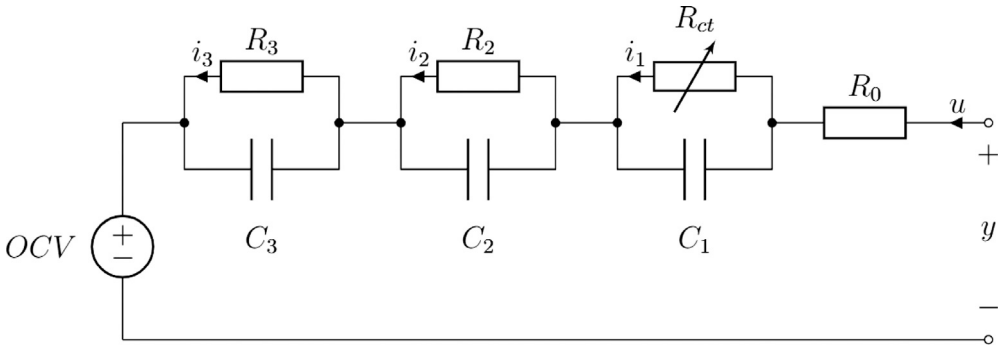

Fig. 3. Equivalent circuit model employed in this article.

where α is the electrode charge transfer coefficient, i_0 is the exchange current density and F and R_g stand for the Faraday constant and the universal gas constant, respectively, and T is the absolute temperature. Anodic and cathodic reactions are assumed to be symmetric in lithium-ion batteries, therefore α is estimated to be 0.5. Therefore, the Butler–Volmer equation can be further simplified to:

$$i = 2i_0 \sinh\left(\frac{F\eta}{2R_gT}\right) \tag{2}$$

The charge transfer resistance R_{ct} is defined as the quotient between overpotential and current. Consequently, the current dependence of the charge-transfer resistance can be expressed as follows:

$$R_{ct}(i_{Rct}) = R_{ct,0}\frac{\sinh^{-1}\left(\frac{i_{Rct}}{2i_0}\right)}{\frac{i_{Rct}}{2i_0}} = R_{ct,0}\frac{\sinh^{-1}\left(Ki_{Rct}\right)}{Ki_{Rct}}, \tag{3}$$

where $R_{ct,0}$ (R_1 from now on) is the value of the charge transfer resistance at zero current and $K = 1/2i_0$ is left as a parameter to be estimated. The remaining RC-elements with slower time constants τ_2 and τ_3 are associated with slower diffusion processes of lithium intercalation and deintercalation in the electrodes [26].

Taking the current dependence into account allows for a more comprehensive and physics-informed model [30], while only introducing one additional parameter and an explicit functional dependence that can easily be handled by a Dual Extended Kalman Filter [33]. Furthermore, it is appropriate to consider parameter K in an adaptive manner since the exchange current density i_0 changes for different temperatures and may decrease significantly over the battery lifetime [54] due to the influence of SEI growth on Butler–Volmer kinetics.

The described equivalent circuit model can be expressed in a state-space representation where the input is battery current u_k (positive for charging), the output is terminal voltage and the state variables are the state of charge and RC resistor currents:

$$x = \begin{bmatrix} SOC & i_1 & i_2 & i_3 \end{bmatrix}^T \tag{4}$$

The discrete-time update equations for the state variables are presented in Eq. (5). Choosing currents instead of voltages as state variables as well as time constants rather than capacitances produces linear state equations that depend on only one parameter each. This will result in a simpler implementation of the Dual Extended Kalman Filter.

$$\begin{aligned} SOC_k &= SOC_{k-1} + \tfrac{\Delta t}{Q}u_{k-1} \\ i_{1,k} &= \exp\left(-\tfrac{\Delta t}{\tau_1}\right)i_{1,k-1} + \left(1-\exp\left(-\tfrac{\Delta t}{\tau_1}\right)\right)u_{k-1} \\ i_{2,k} &= \exp\left(-\tfrac{\Delta t}{\tau_2}\right)i_{2,k-1} + \left(1-\exp\left(-\tfrac{\Delta t}{\tau_2}\right)\right)u_{k-1} \\ i_{3,k} &= \exp\left(-\tfrac{\Delta t}{\tau_3}\right)i_{3,k-1} + \left(1-\exp\left(-\tfrac{\Delta t}{\tau_3}\right)\right)u_{k-1} \end{aligned} \tag{5}$$

The output equation expresses the battery voltage as a function of the state variables and circuit parameters, reflecting the OCV-SOC relationship as well as the current dependence of the charge transfer resistance:

$$y_k = OCV(SOC_k) + R_0u_k + R_1\frac{\sinh^{-1}\left(Ki_{1,k}\right)}{K} + R_2i_{2,k} + R_3i_{3,k} \tag{6}$$

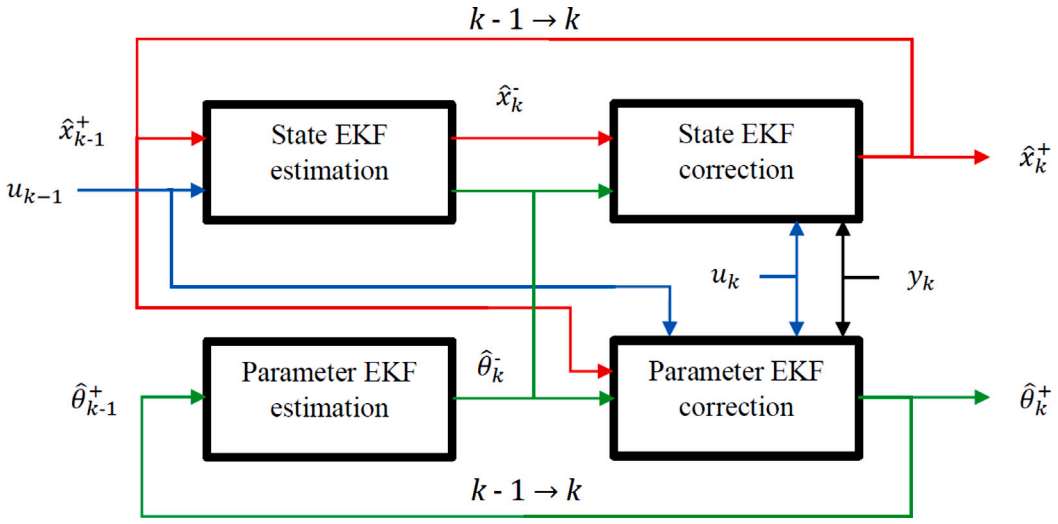

Fig. 4. Flowchart of a Dual Extended Kalman Filter.

3.2. Dual Extended Kalman Filter

The presented equivalent circuit model and its state-space representation allow for the implementation of an Extended Kalman Filter (EKF) with the purpose of SOC estimation providing that input and output measurements are available. Nonetheless, model parameters are not constants since there may be undetected SOC or temperature dependencies as well as internal resistance growth due to cell operation. Therefore, the time-invariant modeling of these parameters produces a continuously increasing process error within the filter, which poses long-term stability and convergence concerns. The Dual Extended Kalman Filter (DEKF) consists of two EKFs in a parallel configuration as shown in Fig. 4, for the simultaneous estimation of both states and parameters, and its general formulation is [40]:

$$\begin{aligned} x_k &= f(x_{k-1}, u_{k-1}, \theta_k) + w_k \\ y_k &= h(x_k, u_k, \theta_k) + v_k \\ \theta_k &= \theta_{k-1} + r_k \\ d_k &= h(x_k, u_k, \theta_k) + e_k, \end{aligned} \tag{7}$$

where x_k is the state vector, u_k is the model input, θ_k is the vector containing the parameters to be estimated and y_k is the model output. f and h are non-linear functions that update the current state and output, meanwhile w_k and v_k are the zero-mean process and measurement noises of covariance Q_k^x and R_k^x, respectively. Given that model parameters are assumed to change in a much slower fashion compared to state dynamics, their fluctuations are attributed to noise r_k with covariance Q_k^θ. The parameter output equation d_k is the same as the state output equation, with noise e_k of covariance R_k^θ.

Following state and parameter initialization, the operation of the DEKF can be summarized in four steps:

1. **Parameter EKF estimation**. The updated *a priori* parameter estimate is equal to the previous *a posteriori* parameter estimate, along with an increase in uncertainty owing to process noise r_k, which is captured in the state error covariance matrix $P_{\theta,k}^-$:

$$\begin{aligned} \hat{\theta}_k^- &= \hat{\theta}_{k-1}^+ \\ P_{\theta,k}^- &= P_{\theta,k-1}^+ + Q_k^\theta \end{aligned} \tag{8}$$

2. **State EKF estimation**. The state and output estimates are updated according to nonlinear functions f and h. State uncertainty increases due to the presence of process noise of covariance Q_k^x:

$$\begin{aligned} \hat{x}_k^- &= f(\hat{x}_{k-1}^+, u_{k-1}, \hat{\theta}_k^-) \\ P_{x,k}^- &= F_{k-1}^x P_{x,k-1}^+ \left(F_{k-1}^x\right)^T + Q_k^x \\ \hat{y}_k &= h(\hat{x}_k^-, u_k, \hat{\theta}_k^-), \end{aligned} \tag{9}$$

where

$$F_{k-1}^x = \left.\frac{\partial f(x_{k-1}, u_{k-1}, \hat{\theta}_k^-)}{\partial x_{k-1}}\right|_{x_k = \hat{x}_{k-1}^+} \tag{10}$$

3. **State EKF correction**. State observer gain L_k^x is calculated and state estimate is corrected by the innovation term, reducing the corresponding uncertainty.

$$\begin{aligned} L_k^x &= P_{x,k}^- \left(H_k^x\right)^T \left(H_k^x P_{x,k}^- \left(H_k^x\right)^T + R_k^x\right) \\ \hat{x}_k^+ &= \hat{x}_k^- + L_k^x \left(y_k - \hat{y}_k\right) \\ P_{x,k}^+ &= \left(I - L_k^x H_k^x\right)^T P_{x,k}^- \left(I - L_k^x H_k^x\right) + L_k^x R_k^x \left(L_k^x\right)^T, \end{aligned} \tag{11}$$

where

$$H_k^x = \left.\frac{\partial h(x_k, u_k, \hat{\theta}_k^-)}{\partial x_k}\right|_{x_k = \hat{x}_k^-} \tag{12}$$

4. **Parameter EKF correction**. Parameter observer gain L_k^θ is calculated and parameter estimate is corrected by the innovation term, reducing the corresponding uncertainty.

$$\begin{aligned} L_k^\theta &= P_{\theta,k}^- \left(H_k^\theta\right)^T \left(H_k^\theta P_{\theta,k}^- \left(H_k^\theta\right)^T + R_k^\theta\right) \\ \hat{\theta}_k^+ &= \hat{\theta}_k^- + L_k^\theta \left(d_k - \hat{d}_k\right) \\ P_{\theta,k}^+ &= \left(I - L_k^\theta H_k^\theta\right)^T P_{\theta,k}^- \left(I - L_k^\theta H_k^\theta\right) + L_k^\theta R_k^\theta \left(L_k^\theta\right)^T, \end{aligned} \tag{13}$$

where

$$H_k^\theta = \left.\frac{dh(\hat{x}_k^+, u_k, \theta_k)}{d\theta_k}\right|_{\theta_k = \hat{\theta}_k^-} \tag{14}$$

The corrected error covariance matrices are expressed in Joseph form to improve the numerical stability of the algorithm [40]. It has to be pointed out that the calculation of matrix H_k^θ requires the computation of the total differential of the model output equation with respect to parameters. For this reason, the total derivative has to be

decomposed into partial derivatives as follows:

$$H_k^{\theta} = \left.\frac{dh(\hat{x}_k, u_k, \theta_k)}{d\theta_k}\right|_{\theta_k=\hat{\theta}_k^-} = \frac{\partial h(\hat{x}_k, u_k, \hat{\theta}_k^-)}{\partial \hat{\theta}_k^-} + \frac{\partial h(\hat{x}_k^-, u_k, \hat{\theta}_k^-)}{\partial \hat{x}_k^-}\frac{d\hat{x}_k^-}{d\hat{\theta}_k^-} \tag{15}$$

$$\frac{d\hat{x}_k^-}{d\hat{\theta}_k^-} = \frac{\partial f(\hat{x}_{k-1}^+, u_{k-1}, \hat{\theta}_k^-)}{\partial \hat{\theta}_k^-} + \frac{\partial f(\hat{x}_{k-1}^+, u_{k-1}, \hat{\theta}_k^-)}{\partial \hat{x}_{k-1}^+}\frac{d\hat{x}_{k-1}^+}{d\hat{\theta}_k^-} \tag{16}$$

$$\frac{d\hat{x}_{k-1}^+}{d\hat{\theta}_k^-} = \frac{d\hat{x}_{k-1}^-}{d\hat{\theta}_{k-1}^+} - L_{k-1}^x \frac{dh(\hat{x}_{k-1}^-, u_{k-1}, \hat{\theta}_{k-1}^+)}{d\hat{\theta}_{k-1}^+} \tag{17}$$

For this purpose, $\frac{d\hat{x}_{k-1}^+}{d\hat{\theta}_k^-}$ is initialized to zero and the three total-derivatives are updated recursively.

Regarding the equivalent circuit model presented in Section 3.1, the parameter vector to be estimated contains the resistors, time constants and the current dependence constant K:

$$\theta = \begin{bmatrix} R_0 & R_1 & R_2 & R_3 & \tau_1 & \tau_2 & \tau_3 & K \end{bmatrix}^T \tag{18}$$

According to the state and output Eqs. (5) and (6), Jacobian matrices required in Eqs. (10), (12), (15) and (16) are the following:

$$F_{k-1}^x = diag\left[1 \quad \exp\left(-\frac{\Delta t}{\hat{\tau}_{1,k}^-}\right) \quad \exp\left(-\frac{\Delta t}{\hat{\tau}_{2,k}^-}\right) \quad \exp\left(-\frac{\Delta t}{\hat{\tau}_{3,k}^-}\right)\right] \tag{19}$$

$$H_k^x = \left[\left.\frac{\partial OCV}{\partial SOC}\right|_{S\hat{O}C_k^-} \quad \frac{\hat{R}_{1,k}^-}{\sqrt{1+(\hat{K}_k^-)^2(\hat{i}_{1,k}^-)^2}} \quad \hat{R}_{2,k}^- \quad \hat{R}_{3,k}^-\right] \tag{20}$$

$$\frac{\partial h(\hat{x}_k, u_k, \hat{\theta}_k^-)}{\partial \hat{\theta}_k^-} = \left[i_k \quad \frac{\sinh^{-1}(\hat{K}_k^-\hat{i}_{1,k}^-)}{\hat{K}_k^-} \quad \hat{i}_{2,k}^- \quad \hat{i}_{3,k}^- \quad 0 \quad 0 \quad 0 \quad \hat{R}_{1,k}^- \frac{\frac{\hat{K}_k^-\hat{i}_{1,k}^-}{\sqrt{1+(\hat{K}_k^-)^2(\hat{i}_{1,k}^-)^2}} - \sinh^{-1}(\hat{K}_k^-\hat{i}_{1,k}^-)}{(\hat{K}_k^-)^2}\right] \tag{21}$$

$$\frac{\partial f(\hat{x}_{k-1}^+, u_{k-1}, \hat{\theta}_k^-)}{\partial \hat{\theta}_k^-} = \begin{bmatrix} 0 & 0 & 0 & 0 & 0 & 0 & 0 & 0 \\ 0 & 0 & 0 & 0 & A_1 & 0 & 0 & 0 \\ 0 & 0 & 0 & 0 & 0 & A_2 & 0 & 0 \\ 0 & 0 & 0 & 0 & 0 & 0 & A_3 & 0 \end{bmatrix} \tag{22}$$

Where:

$$\begin{aligned} A_1 &= \frac{\Delta t}{(\hat{\tau}_{1,k}^-)^2}\exp\left(-\frac{\Delta t}{\hat{\tau}_{1,k}^-}\right)\left(\hat{i}_{1,k-1}^+ - u_{k-1}\right) \\ A_2 &= \frac{\Delta t}{(\hat{\tau}_{2,k}^-)^2}\exp\left(-\frac{\Delta t}{\hat{\tau}_{2,k}^-}\right)\left(\hat{i}_{2,k-1}^+ - u_{k-1}\right) \\ A_3 &= \frac{\Delta t}{(\hat{\tau}_{3,k}^-)^2}\exp\left(-\frac{\Delta t}{\hat{\tau}_{3,k}^-}\right)\left(\hat{i}_{3,k-1}^+ - u_{k-1}\right) \end{aligned} \tag{23}$$

Once the theoretical framework for the DEKF has been established, the algorithm is initialized by inputting the starting values for both states and parameters. Given that the cycling scheme begins with a short rest period, initial SOC is estimated via voltage measurement and the OCV-SOC relationship; meanwhile initial currents are set to zero:

$$\hat{x}_0^+ = \begin{bmatrix} OCV^{-1}(v_0) & 0 & 0 & 0 \end{bmatrix}^T \tag{24}$$

Therefore, the state estimation error covariance matrix is initialized as:

$$\hat{P}_0^x = diag\begin{bmatrix} 10^{-3} & 0 & 0 & 0 \end{bmatrix} \tag{25}$$

Initial equivalent circuit parameters are obtained from the internal resistance test carried out during the first RPT (Fig. 2). R_0 is calculated as the quotient $\Delta V/\Delta I$ at the beginning of every peak ±C/2 current pulse [52]. Next, the voltage transients are employed to obtain the RC network parameters. For this purpose, the initial voltage step is subtracted and the remaining transient is fitted to a 3-exponential response via a non-linear least squares algorithm. This calculation was carried out for the three intermediate SOCs both for charge and discharge, with a resulting R^2 over 0.999 in all cases. Representative values for each parameter are calculated as the average of all cases. Meanwhile parameter K from the current dependence is initialized to 0.1 [54]. Therefore, the initial parameter vector is expressed in Eq. (26):

$$\hat{\theta}_0^+ = \begin{bmatrix} 0.0272 & 0.01525 & 0.0162 & 0.0052 & 22.51 & 184.2 & 2064.6 & 0.1 \end{bmatrix}^T \tag{26}$$

On the other hand, the parameter estimation error covariance matrix is initially set to a diagonal matrix with parameter variances calculated in the previous step and then manually adjusted. The error covariance of parameter K is estimated to be 0.1.

$$\hat{P}_0^{\theta} = diag\begin{bmatrix} 10^{-7} & 10^{-7} & 10^{-7} & 10^{-7} & 0.1 & 1 & 10 & 0.1 \end{bmatrix} \tag{27}$$

In order to ensure the stability and convergence of the state and parameter filters, tuning the covariance matrices corresponding to process and measurement noises of both state and parameter filters Q_0^x, R_0^x Q_0^{θ} and R_0^{θ} is required. Parameter covariances are set to reduced values so as to capture long-term variations due to degradation and not quick changes that could imply overfitting. In this case, covariance matrices have been initialized to the following values:

$$\begin{aligned} Q_k^x &= 10^{-6}\cdot diag\begin{bmatrix} 0.1 & 1 & 1 & 1 \end{bmatrix} \\ Q_k^{\theta} &= 10^{-10}\cdot diag\begin{bmatrix} 1 & 1 & 1 & 1 & 10 & 100 & 1000 & 10 \end{bmatrix} \\ R_k^x &= 10^{-2} \qquad R_k^{\theta} = 10^{-2} \end{aligned} \tag{28}$$

4. SOH estimation

As presented in [41] and Section 1, the long-term state of health estimation by including capacity as a parameter in the DEKF algorithm entails serious reliability concerns. Moreover, updating capacity every timestep introduces a fair amount of noise in SOC estimation resulting in large fluctuations in electrical parameters as well as in capacity estimates, compromising overall filter stability.

Considering that cell degradation is a slower process than battery dynamics by several orders of magnitude, we develop an approach based on [55] to implement the weighted recursive least squares with fading memory (FMWRLS) for long-term capacity estimation. This algorithm outputs an estimate $\hat{Q}$ such that $y \approx \hat{Q}x$ using vectors of measured data x and y, where x_i is the estimated change in state-of-charge and y_i is the change in electrical charge in Ah over interval i with start and finish points t_1 and t_2.

$$\begin{aligned} x_i &= S\hat{O}C(t_2) - S\hat{O}C(t_1) \\ y_i &= \sum_{k_1}^{k_2} u_k \Delta t_k, \end{aligned} \tag{29}$$

where k_1 and k_2 correspond to t_1 and t_2, respectively. SOC corrected estimations (11) provided by the DEKF described in Section 3.2 contain enough voltage feedback so that the equation $y \approx \hat{Q}x$ does not become an identity. The estimate $\hat{Q}$ minimizes the sum of weighted squared errors, where the weighting takes into account the uncertainty of each accumulated charge measurement.

The equations for the recursive implementation of FMWRLS are the following:

$$\begin{aligned} c_{1,n} &= \gamma c_{1,n-1} + \frac{x_n^2}{\sigma_{y,n}^2} \\ c_{2,n} &= \gamma c_{2,n-1} + \frac{x_n y_n}{\sigma_{y,n}^2} \\ \hat{Q}_n &= \frac{c_{2,n}}{c_{1,n}}, \end{aligned} \tag{30}$$

where γ is the forgetting factor, which has been set to 0.986. This is the value that provides the closest match between the estimated remaining capacity and the experimental measurements. Fading memory

of past capacity estimates is included to give a greater weight to recent estimates, thus allowing $\hat{Q}$ to adjust for actual capacity changes.

Given that a cell with nominal capacity Q_{nom} has said capacity over a state-of-charge range of 1, the algorithm is initialized with these values for x_0 and y_0. On the other hand, $\sigma^2_{y,n}$ is the variance of the nth charge measurement, which is assumed to comprise accumulated quantization noises and may be estimated as the variance of a uniform distribution multiplied by the time interval $t_2 - t_1$ and scaled by the factor 3600^2:

$$\sigma^2_{y,n} = \frac{q^2 \cdot (t_2 - t_1)}{(12 \cdot 3600^2)}, \tag{31}$$

where q is the current sensor effective precision, which in this case has been determined to be 2 mA.

One crucial issue with SOH estimation is at what operating stage and how often new x and y measurements are made. Frequent measurements result in a lower σ^2_y but also a smaller SOC difference, which can make the capacity estimate more susceptible to noise, thus destabilizing the DEKF. In addition to this, carrying out these measurements during high-rate or intermittent discharges may lead to unreliable estimations. For the reasons above, x and y measurements are only made from the start to the end of the CC charging period, which allows for a large SOC increment as well as a more reliable SOC prediction and y measurement given the constant current. Updating capacity once every cycle is deemed adequate to reflect actual variations in capacity without introducing excessive noise in the SOC estimation method. Finally, this procedure is also applicable to other testing schemes as well as real-life battery operation since CC charging periods from 20% SOC to 80% SOC are guaranteed to occur regularly, therefore providing a sufficiently large SOC increment to ensure its correct behavior. This algorithm presents the advantage of providing a closed-form solution for $\hat{Q}$, which can easily be computed in a recursive manner. Furthermore, the forgetting factor γ allows adjusting the relevance of past and recent measurements so that capacity estimates reflect cell degradation.

5. Surface and core temperature estimation

As discussed in Section 1, there has been a recent surge in interest in online temperature estimation via non-intrusive or indirect methods [22,23], due to the inaccessibility of individual cell measurements in practical operation. In this section, we employ a thermal model that relies on the electrical model described in Section 3 for the heat generation term, and only requires ambient temperature measurements to estimate cell surface and core temperatures. The continuous updating and correction of electrical parameters by the DEKF allows this model to remain valid for long-term operation.

As shown by authors [37,56], entropic heat generation can be disregarded without exceeding errors of ±1 °C, which is within the tolerance error range of T-type thermocouples. Under this condition, the estimated heat generation rate is determined as the product of cell current and overvoltage from Eq. (6), with corrected parameters and states from the DEKF being used for this calculation every timestep.

$$\begin{aligned}\hat{P}_{J,k} &= u_k[y_k - OCV(S\hat{O}C_k)] = \\ &= \hat{R}^+_{0,k}u_k^2 + \hat{R}^+_{1,k}u_k\frac{\sinh^{-1}(\hat{K}^+_k\hat{\imath}^+_{1,k})}{\hat{K}^+_k} + \hat{R}^+_{2,k}u_k\hat{\imath}^+_{2,k} + \hat{R}^+_{3,k}u_k\hat{\imath}^+_{3,k}\end{aligned} \tag{32}$$

Once the heat generation term has been defined, the thermal model is introduced. As stated in Section 1, the 1-D heat equation of a cylinder may be reduced to a system of ODEs by assuming a polynomial temperature profile with the radial spatial variable r. The approximation with a fourth-order polynomial was presented and derived in [57], yielding a state-space representation whose state variables are the averaged temperature and temperature gradients, whereas its inputs are the heat generation rate and the ambient temperature and its outputs are the core and surface temperatures. However, in said work, the heat generation was calculated directly from experimental measurements of terminal voltage and current, as well direct SOC calculations via Coulomb counting. Conversely, in this article, it is calculated as the resistive heat generated according to an adaptive electrical model. We consider this to be a qualitative advantage since it allows the thermal model to remain usable in the long term due to the continuous updating of electrical parameters.

If the changes in the ambient temperature are presumed to happen in a much slower timescale than the thermal dynamics of the cell, which is typically true, their effects on temperature increments may be safely neglected. This is equivalent to assuming that the ambient temperature remains approximately constant throughout the cell thermal transients, which allows for the reduction of the thermal model and the consideration of the ambient temperature as a direct term in the subsequent state-space representation. As a result of this, the transfer functions from the heat generation rate to the surface and core temperatures are equivalent to those where the outputs are the temperature increment with respect to the environment $T_{CA}(s)$, $T_{SA}(s)$ [57]:

$$\frac{T_{CA}(s)}{P_J(s)} = \frac{1}{hA}\frac{s\left[\frac{R^2}{20\alpha_t} - \frac{hR^3}{160k_t\alpha_t}\right] + 1 + \frac{hR}{2k_t}}{s^2\left[\frac{R^4}{960\alpha_t^2} + \frac{k_tR^3}{20h\alpha_t^2}\right] + s\left[\frac{7R^4}{40\alpha_t} + \frac{k_tR}{2h\alpha_t}\right] + 1} \tag{33}$$

$$\frac{T_{SA}(s)}{P_J(s)} = \frac{1}{hA}\frac{s\frac{R^2}{20\alpha_t} + 1}{s^2\left[\frac{R^4}{960\alpha_t^2} + \frac{k_tR^3}{20h\alpha_t^2}\right] + s\left[\frac{7R^4}{40\alpha_t} + \frac{k_tR}{2h\alpha_t}\right] + 1} \tag{34}$$

where h is the convection coefficient, k_t is the cell average thermal conductivity, α_t is the cell average thermal diffusivity, A is the cell lateral surface area and R is the cell radius.

An alternative choice would have been to employ a 2RC Cauer network for the thermal model, such as in [58]. However, the resulting transfer functions present four free parameters corresponding to two resistors (R_{CS}, R_{SA}) and two capacitors (C_{CA}, C_{SA}) whose values may not have a clear physical interpretation. Conversely, since the cell dimensions are known, the transfer functions in Eqs. (33) and (34) only have three fitting physical parameters (h, k_t and α_t), whose range of values have been experimentally measured in previous works [18]. Furthermore, the transfer function from the heat generation rate to the surface temperature increment is not exactly equivalent. For these reasons, the reduced order model has been employed in this study.

The parameter values are determined by means of the thermal characterization test described in Section 2. For this purpose, the electrical model described in Section 3 is simulated and the heat generation term is estimated according to Eq. (32), while the modeled surface temperature increment is adjusted to its experimental value. The identification result is shown in Fig. 5.

The identified parameter values are $h = 33.18$ W/m^2°C, $k_t = 0.64$ W/m°C and $\alpha_t = 1.59 \cdot 10^{-7}$m^2/s, which are in agreement with those obtained in previous works [18]. These parameters are expected to remain stable during the cell lifetime as long as the environment and the cell arrangement are maintained [58].

The zero-pole representation of Eqs. (33) and (34) are the following:

$$\frac{T_{CA}(s)}{P_J(s)} = \frac{10.11(19.45s + 1)}{(23.16s + 1)(612s + 1)} \tag{35}$$

$$\frac{T_{SA}(s)}{P_J(s)} = \frac{8.2(25.47s + 1)}{(23.16s + 1)(612s + 1)} \tag{36}$$

In light of these results, it is observed that a nearly exact zero-pole cancellation may be carried out. Therefore, a dominant pole approximation can be done with barely any loss of accuracy. The Bode plots of both transfer functions and their approximations are shown in Figs. 6 and 7.

The dominant pole approximation makes it possible to use the transfer functions and physically significant thermal parameters mentioned above to achieve a reduced-order model that allows for a simpler

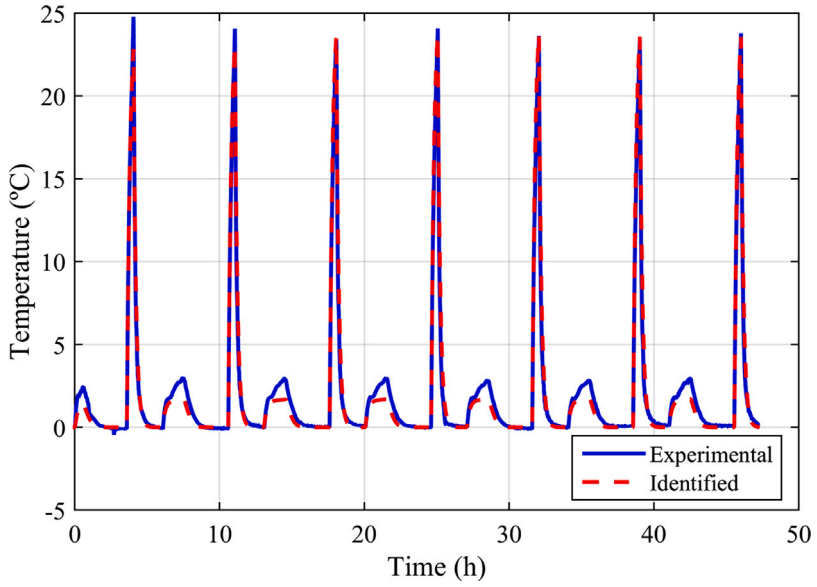

Fig. 5. Experimental and identified surface temperature increment during the thermal characterization test.

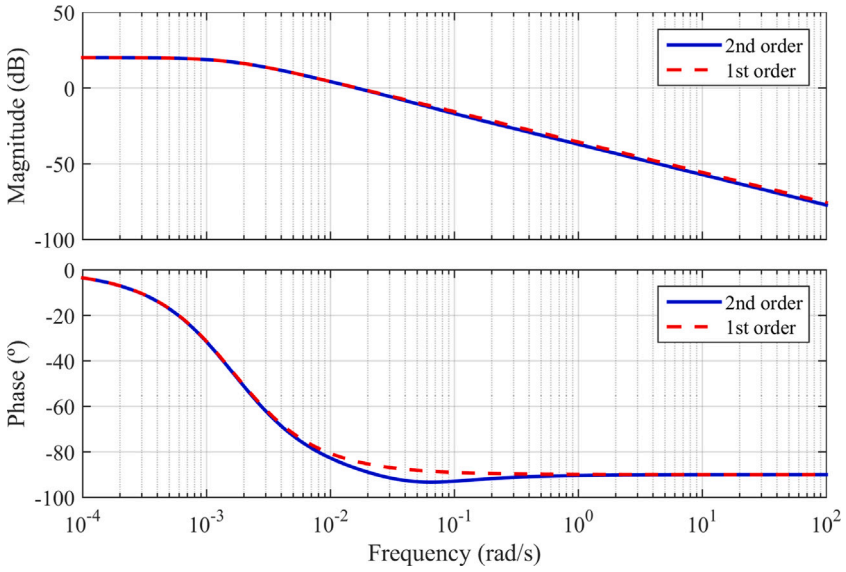

Fig. 6. Second-order transfer function and first order approximation for the core temperature increment.

state-space implementation. This is necessary so as to facilitate the simulation in the time domain with a variable sampling period, which is a common occurrence in long-term battery operation. Consequently, the following lumped parameters may be identified in the approximate model:

$$R_{SA} = 8.2\ ^{\circ}\text{C/W}, \quad R_{CS} = 1.91^{\circ}\text{C/W}, \quad \tau_{th} = 612\ \text{s} \tag{37}$$

Finally, the simplified discrete state-space representation of the thermal model is as follows:

$$\begin{bmatrix}\hat{T}_{CA,k}\\ \hat{T}_{SA,k}\end{bmatrix} = \begin{bmatrix}\exp\left(-\frac{\Delta t}{\tau_{th}}\right) & 0\\ 0 & \exp\left(-\frac{\Delta t}{\tau_{th}}\right)\end{bmatrix}\begin{bmatrix}\hat{T}_{CA,k-1}\\ \hat{T}_{SA,k-1}\end{bmatrix} + \begin{bmatrix}(R_{CS}+R_{SA})\left(1-\exp\left(-\frac{\Delta t}{\tau_{th}}\right)\right) & 0\\ R_{SA}\left(1-\exp\left(-\frac{\Delta t}{\tau_{th}}\right)\right) & 0\end{bmatrix}\begin{bmatrix}\hat{P}_{J,k-1}\\ T_{A,k-1}\end{bmatrix} \tag{38}$$

$$\begin{bmatrix}\hat{T}_{C,k}\\ \hat{T}_{S,k}\end{bmatrix} = \begin{bmatrix}1 & 0\\ 0 & 1\end{bmatrix}\begin{bmatrix}\hat{T}_{CA,k}\\ \hat{T}_{SA,k}\end{bmatrix} + \begin{bmatrix}0 & 1\\ 0 & 1\end{bmatrix}\begin{bmatrix}\hat{P}_{J,k-1}\\ T_{A,k}\end{bmatrix},$$

where the model inputs are the estimated heat generation rate and the ambient, while the outputs are the estimated core and surface temperatures.

6. Results and discussion

In this section, the simulation results obtained by applying the models described in Sections 3–5 are validated against experimental measurements. First, voltage, SOC and temperature estimations are compared to their corresponding experimental values. Estimation results are shown in Figs. 8–10 for several cycles at three significant stages during cell lifetime, namely cycles 198–200, 498–500 and 798–800. It has to be noted that the time indicated in the x-axis corresponds to the number of hours since the start of that particular duty cycling scheme (i.e., Block IV), as described in the Experimental section.

Root-mean-square error (RMS) and mean-absolute error (MAE) between predictions and experimental data for every stage of cycling are summarized in Table 1. It has to be pointed out that the proposed

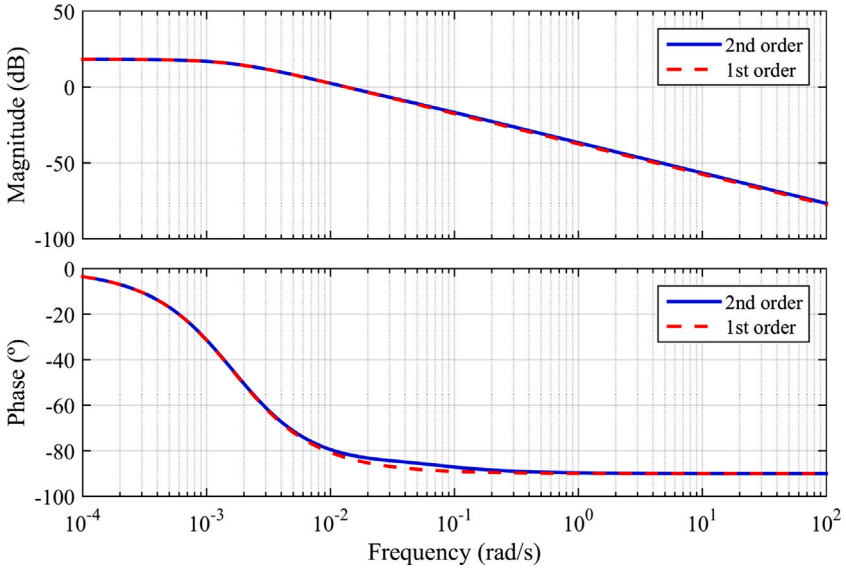

Fig. 7. Second-order transfer function and first order approximation for the surface temperature increment.

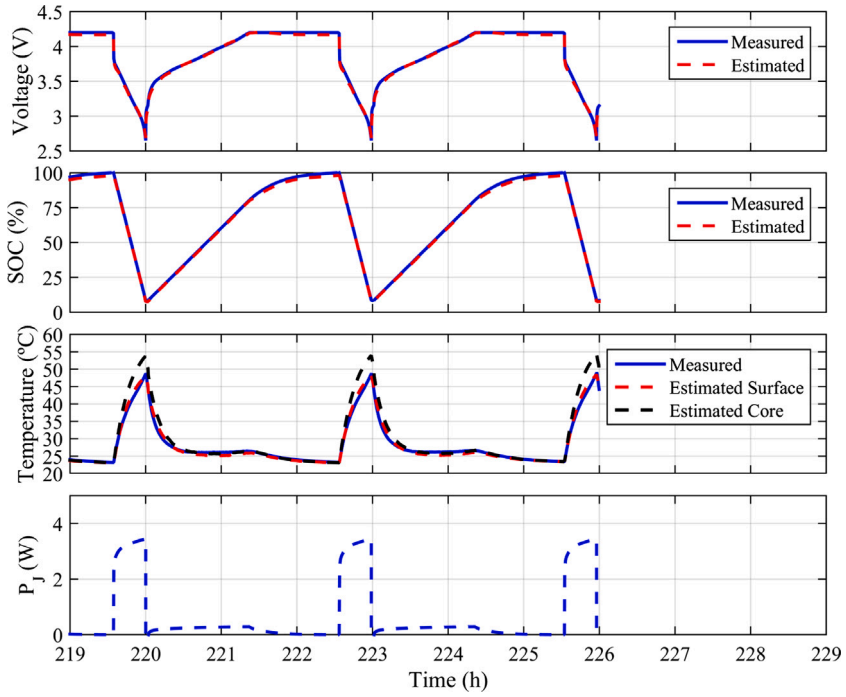

Fig. 8. Voltage, SOC and temperature measurements and estimations for cycles 198–200.

method gives a MAE below 25.8 mV for cell voltage, 1.82% for cell SOC and 0.88 °C for surface temperature.

Regarding temperature estimation, the proposed model accurately reflects cell thermal behavior: as shown in Figs. 8–10, both temperature rise and relaxation profiles as well as peaks are correctly matched. The temperature estimation shows minor disagreements with the experimental results during the CC charging stage. These temperature differences may be caused by additional sources of heat generation, such as entropic heat [59], which may be overshadowed by the 2C discharges and only become apparent at low current rates. Still, the estimated temperature on the CV stage is never above 1.5 °C, which is within the accuracy range of the T-type thermocouples employed in the experimental schemes. That leads to conclude that a more complex thermal model would not provide significant improvements

Table 1
Summary of estimation results.

Error	Voltage (mV)		SOC (%)		Surface temperature (°C)	
Cycle	RMS	MAE	RMS	MAE	RMS	MAE
0–100	25.1	19.0	1.58	1.44	1.08	0.83
100–200	24.2	18.5	1.24	1.15	0.93	0.74
200–300	26.0	19.4	1.38	1.24	1.07	0.75
300–400	26.3	20.3	1.82	1.51	0.99	0.87
400–500	26.6	20.7	0.52	0.41	0.82	0.65
500–600	28.9	21.4	1.07	0.96	0.84	0.67
600–700	31.6	23.4	0.80	0.66	0.86	0.68
700–800	33.9	25.8	1.08	0.83	0.97	0.75

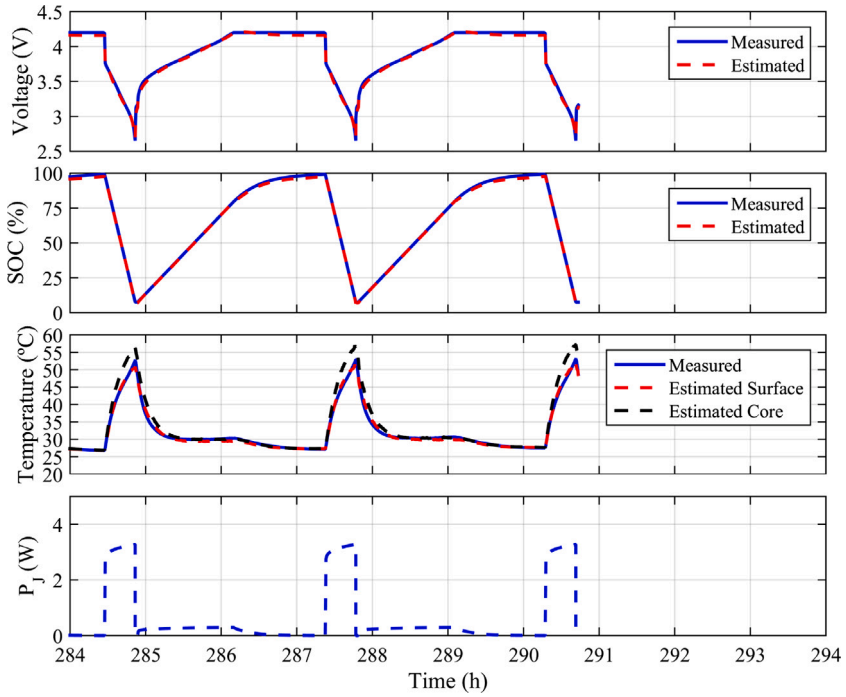

Fig. 9. Voltage, SOC and temperature measurements and estimations for cycles 498–500.

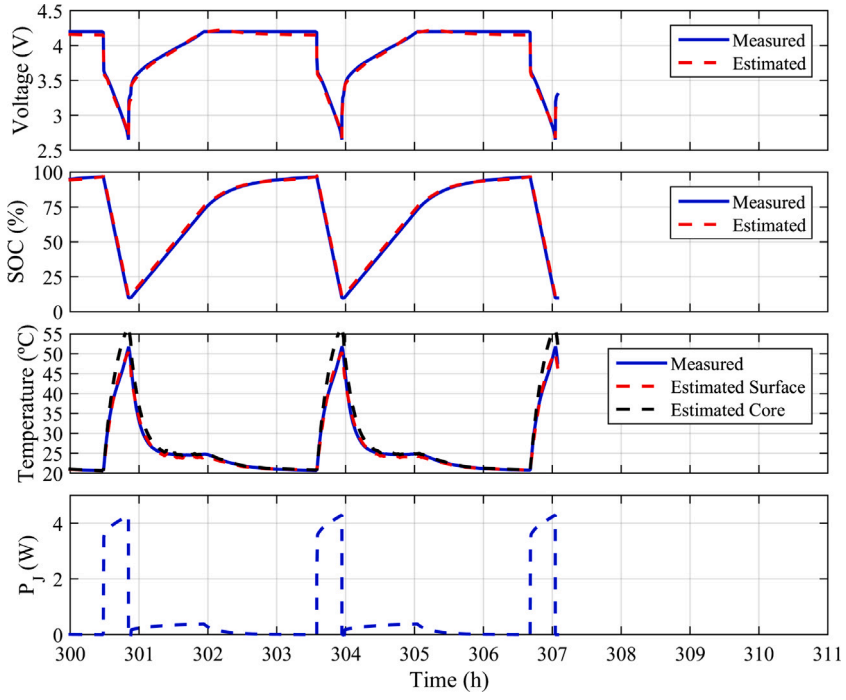

Fig. 10. Voltage, SOC and temperature measurements and estimations for cycles 798–800.

regarding the temperature estimation. The great agreement between estimated and measured temperature also serves to validate the electrical model since the heat generation term relies on the continuous updating and correction of electrical parameters. The results provided by the proposed method cannot be compared directly to those from previous works, such as [58], given that the considered time frames are notably distinct i.e., a drive cycle and the lifetime of the studied cell. Furthermore, drive cycles consist of high frequency current signals, so the complete thermal transient response and relaxation profile may not be taken into account when carrying out the error analysis. As discussed in Section 1, Ludwig et al. [22] recently proposed a sensorless method for online resistance-based temperature estimations with empirical expressions for the updating of electrical parameters, yielding an RMS error below 1.2 °C for as long as 200 cycles. Our integrated approach provides estimation results with the same degree of accuracy throughout 800 cycles without the need for *a priori* knowledge of the long-term behavior of the electrical parameters.

Furthermore, the accurate estimations of surface temperature also serve to validate the parameterization procedure for the thermal model.

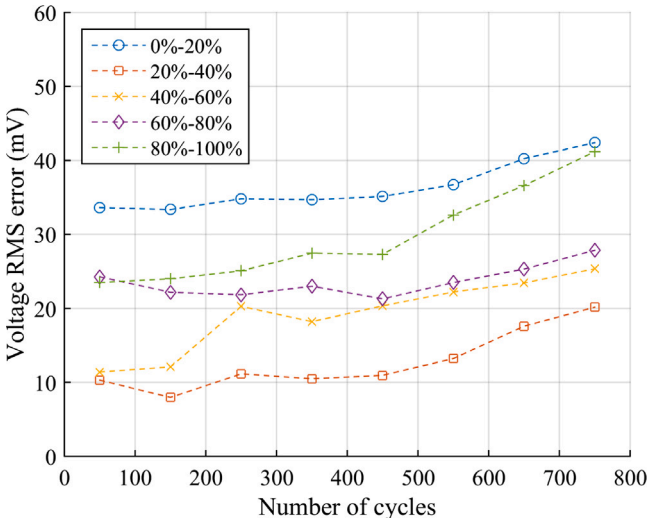

Fig. 11. Voltage estimation performance for different SOC ranges.

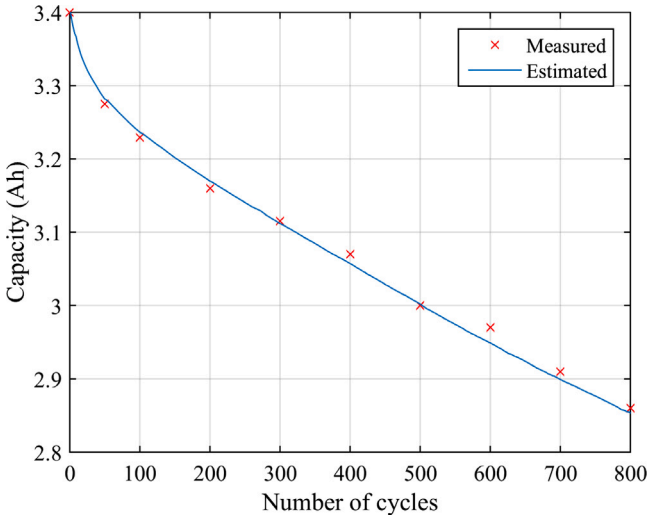

Fig. 12. Measured and estimated cell capacity.

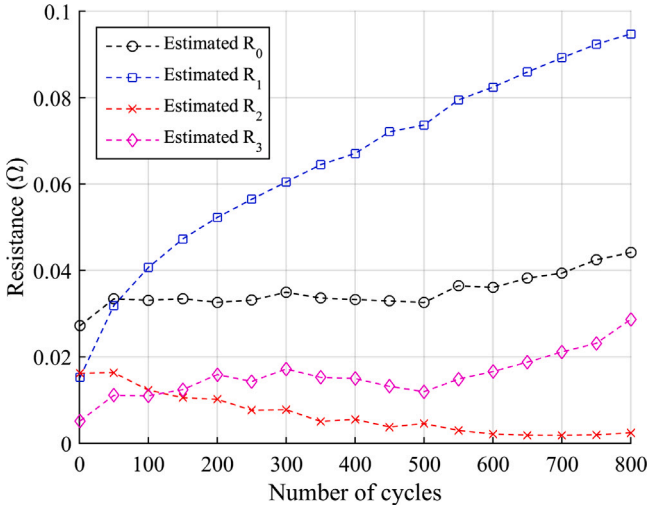

Fig. 13. Estimated resistor values during cycling.

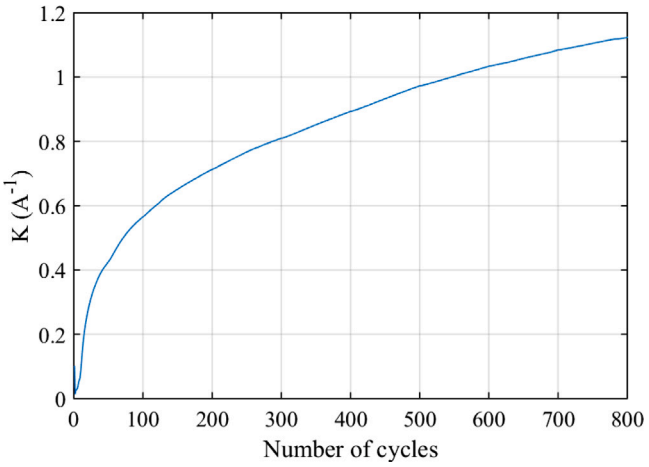

Fig. 14. Estimated parameter K during cycling.

Given that the identified parameters have a clear physical interpretation and their values are within previously experimentally determined ranges [18], the core temperature estimation may be considered to be representative of the inner temperature distribution. Additionally, the core temperature is estimated to be 4 °C to 6 °C above the surface temperature at the end of the 2C discharge according to this method, which is in line with previous works in which the internal temperature is measured experimentally [60,61]. Nevertheless, inserting an internal temperature sensor into the cell under test is highly invasive procedure, therefore possibly interfering with the internal structure and arrangement of the cell and, consequently, affecting its behavior as shown by Chen et al. [61] and Huang. et al. [60] and compromising its long-term stability and reliability. Moreover, it is not straightforward to determine which section and material of the cell the sensor is in direct contact with, so it may not be possible to elucidate whether the measured temperature is in agreement with the theoretical temperature at $r = 0$. In summary, we believe the main advantage of the proposed method to be the ability to accurately estimate the surface temperature of the cell, as well as provide a representative value of its internal temperature throughout its lifetime without the need for physical sensors, given that the assumption of a homogeneous cell temperature may not hold at moderate to high current rates [62].

The accurate temperature estimations are due to the precise SOC and voltage estimations. As shown in Figs. 8–10, the DEKF provides a voltage estimation which is in great agreement with experimental measurements through both discharges and the constant-current stages of charging. The largest deviation from the measured values is reached in the CV stages, because during this stage the voltage becomes the actual input of the model and the cell current turns into the output. Nevertheless, estimation errors in these phases are less critical since the cell operates in thoroughly controlled conditions. Fig. 11 shows the evolution with cycling of the voltage estimation evaluated at different SOC ranges. The voltage estimation steadily loses accuracy as the number of cycles increases and the cell ages, showing larger errors in the lowest and highest SOC range and a better performance over central SOCs. This is an expected result owing to changes in the electrode open circuit potential (OCP) curves, and consequently the resulting OCV-SOC relationship, that have been reported at different degradation stages in cells containing Ni-rich, blended Si–Gr anodes [14], which mostly affect the highest and lowest SOC ranges.

Another feature of this work is the SOH estimation. As shown in Fig. 12, estimated capacity via the FMWRLS algorithm closely matches actual capacity measured via RPTs at cycle 50 and then every 100 cycles. The capacity estimation results are in great agreement with the experimental data, with a maximum relative error of 0.61% showing

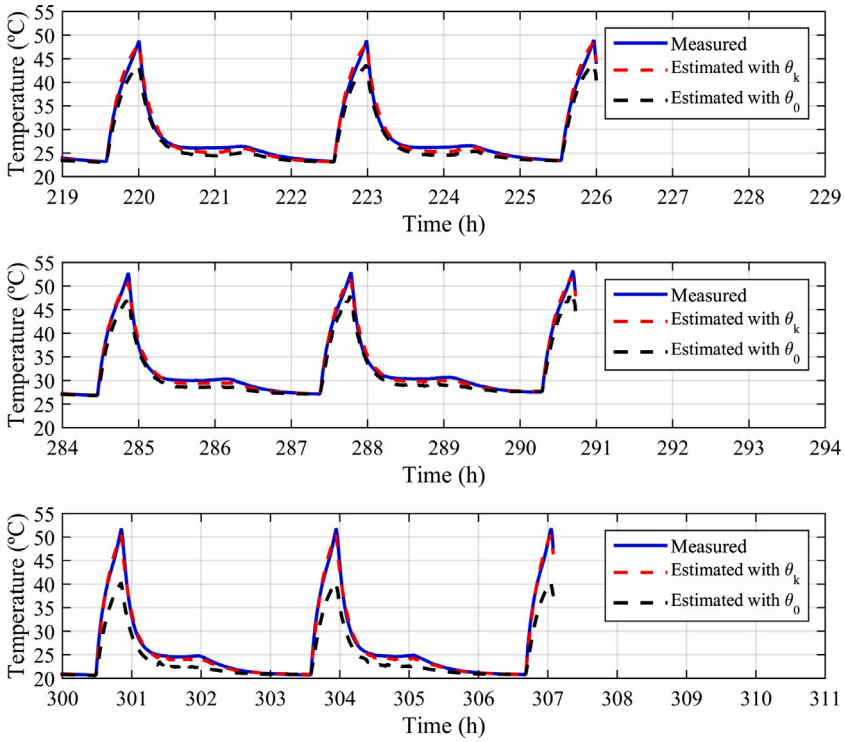

Fig. 15. Measured and estimated surface temperature with and without parameter updating. Top: cycles 198–200. Middle: cycles 498–500. Bottom: cycles 798–800.

Table A.2
Table of abbreviations employed in this article.

Abbreviation	Description
LIB	Lithium-ion battery
NMC811	Nickel–Manganese–Cobalt
Si–Gr	Silicon–Graphite
NCA	Nickel–Cobalt–Aluminium
EV	Electric Vehicle
RUL	Remaining Useful Life
BMS	Battery Management System
EIS	Electrochemical Impedance Spectroscopy
PDE	Partial differential equation
ODE	Ordinary differential equation
SOC	State Of Charge
SOH	State Of Health
ECM	Equivalent Circuit Model
EKF	Extended Kalman Filter
DEKF	Dual Extended Kalman Filter
RLS	Recursive Least Squares
FMWRLS	Fading Memory Weighted Recursive Least Squares
RPT	Reference Performance Test
OCV	Open Circuit Voltage
OCP	Open Circuit Potential
CC-CV	Constant Current - Constant Voltage
RMS	Root Mean Square
MAE	Mean Absolute Error

Table B.3
Nomenclature.

Symbol	Description (Units)
Q, Q_{nom}	Cell capacity, Nominal capacity (Ah)
R_{ct}	Charge-transfer resistance (Ω)
i_0	Exchange current (A)
α	Charge transfer coefficient
F	Faraday's constant (C/mol)
η	Charge transfer reaction overpotential (V)
R_g	Universal gas constant (J/K mol)
T	Temperature (K)
K	Current dependence parameter (A^{-1})
γ	Forgetting factor
q	Current sensor precision (A)
P_J	Heat generation rate (J)
T_{CA}	Core-ambient temperature difference (K)
T_{SA}	Surface-ambient temperature difference (K)
h	Heat transfer coefficient (W/m^2K)
R, A	Cell radius and surface area (m, m^2)
k_t	Cell thermal conductivity (W/mK)
α_t	Cell thermal diffusivity (m^2/s)
R_{SA}	Surface-ambient thermal resistance (K/W)
R_{CS}	Core-surface thermal resistance (K/W)
τ_{th}	Thermal time constant (s)
T_A	Ambient temperature (K)

accuracy improvements with respect to previous works [48], where maximum relative errors reached 2%. It has to be noted that the capacity estimations reflect the nonlinear initial degradation stage, as well as the following linear trend, for nearly the complete lifetime of the cell until a final capacity loss of 15.6% is reached. Accurate capacity estimations prove to be essential to the correct behavior and stability of the filter.

Next, the evolution of the estimated equivalent circuit parameter values is shown in Figs. 13 and 14. It has to be noted that most of the internal resistance increase is ascribed to R_1. Parameter K grows in accordance, which was anticipated in [54]. This demonstrates that the inclusion of the current dependence of the charge transfer resistance, as well as the online estimation of its parameter, greatly improve the performance of the model. Time constants are estimated to remain largely stable during cycling.

Finally, the importance of the online updating of the equivalent circuit parameters is highlighted in Fig. 15. This shows that the peak error in the estimated temperature remains stable below 1.5 °C throughout cell lifetime if electrical parameter are updated, whereas it grows from 4 °C to 12 °C otherwise.

The main drawback of ECMs is usually the lack of the correlation between the circuit elements and the physical and chemical processes occurring in the LIB. This can make the interpretation of the identified parameters ambiguous, thus rendering its analysis unfruitful [63].

However, it is observed that temperature, voltage, SOC and capacity estimations closely match experimental measurements. This is indicative of the fact that open circuit voltage, overvoltage and, consequently, heat generation rate are estimated correctly by the DEKF, and thus serve its intended purpose of battery monitoring, even if the individual parameter values do not reflect the internal behavior of the cell.

7. Conclusions

In this article, the lifetime sensorless estimation of surface and internal temperature has been carried out on a novel NMC811/Si–Gr battery cell. To attain this range of applicability, a complete electro-thermal is developed with the goal of estimating the cell surface and core temperature indirectly when the ambient temperature is available. For this purpose, a physics-informed equivalent circuit model that takes into account the current dependence of the charge transfer resistance has been employed. Parameter values are continuously estimated by means of a Dual Extended Kalman Filter, allowing the electrical model to remain valid in the long term; whereas the remaining capacity is calculated via a Recursive Least Squares algorithm with a forgetting factor. Next, a physics-based reduced-order thermal model is characterized and its parameters are identified. The continuous updating of the equivalent circuit parameters allows the heat generation term and therefore, the temperature estimations, to remain highly accurate with a maximum RMS error of 1.2 °C for as long as 800 complete cycles. The reduced computational cost of the proposed procedure along with its overall satisfactory performance, as well as the sensorless temperature measurement, make it a suitable choice for the online monitoring of battery cells.

CRediT authorship contribution statement

Pablo Rodríguez-Iturriaga: Conceptualization, Methodology, Investigation, Writing – original draft. **David Anseán:** Investigation, Resources, Data curation, Writing – original draft. **Juan Antonio López-Villanueva:** Methodology, Investigation, Writing – review & editing, Supervision. **Manuela González:** Investigation, Resources, Data curation, Supervision. **Salvador Rodríguez-Bolívar:** Conceptualization, Methodology, Investigation, Writing – original draft, Writing – review & editing.

Declaration of competing interest

The authors declare that they have no known competing financial interests or personal relationships that could have appeared to influence the work reported in this paper.

Data availability

Data will be made available on request.

Acknowledgments

This work was partially supported by the Spanish Ministry of Science and Innovation and by FEDER funds via Project MCI-20-PID2019-110955RB-I00, by the Principality of Asturias via project AYUD/2021/50994 and via project P18-RT-3303 by Plan Andaluz de Investigación, Desarrollo e Innovación (PAIDI 2020, Regional Government of Andalusia).

Appendix A. Abbreviations

See Table A.2.

Appendix B. Nomenclature

See Table B.3.

References

[1] G. Zubi, R. Dufo-López, M. Carvalho, G. Pasaoglu, The lithium-ion battery: State of the art and future perspectives, Renew. Sustain. Energy Rev. 89 (2018) 292–308, http://dx.doi.org/10.1016/j.rser.2018.03.002.

[2] D. Stampatori, P.P. Raimondi, M. Noussan, Li-ion batteries: A review of a key technology for transport decarbonization, Energies 13 (10) (2020) http://dx.doi.org/10.3390/en13102638.

[3] S. Chae, S.-H. Choi, N. Kim, J. Sung, J. Cho, Integration of graphite and silicon anodes for the commercialization of high-energy lithium-ion batteries, Angew. Chem., Int. Ed. Engl. 59 (1) (2020) 110–135, http://dx.doi.org/10.1002/anie.201902085.

[4] M.N. Obrovac, L.J. Krause, Reversible cycling of crystalline silicon powder, J. Electrochem. Soc. 154 (2) (2007) A103, http://dx.doi.org/10.1149/1.2402112.

[5] E. Moyassari, L. Streck, N. Paul, M. Trunk, R. Neagu, C.-C. Chang, S.-C. Hou, B. Märkisch, R. Gilles, A. Jossen, Impact of silicon content within silicon-graphite anodes on performance and Li concentration profiles of Li-ion cells using neutron depth profiling, J. Electrochem. Soc. 168 (2) (2021) 020519, http://dx.doi.org/10.1149/1945-7111/abe1db.

[6] F. Benavente-Araoz, M. Varini, A. Lundblad, S. Cabrera, G. Lindbergh, Effect of partial cycling of NCA/Graphite cylindrical cells in different SOC intervals, J. Electrochem. Soc. 167 (4) (2020) 040529, http://dx.doi.org/10.1149/1945-7111/ab78fd.

[7] T.M.M. Heenan, A. Jnawali, M.D.R. Kok, T.G. Tranter, C. Tan, A. Dimitrijevic, R. Jervis, D.J.L. Brett, P.R. Shearing, An advanced microstructural and electrochemical datasheet on 18650 Li-Ion batteries with nickel-rich NMC811 cathodes and graphite-silicon anodes, J. Electrochem. Soc. 167 (14) (2020) 140530, http://dx.doi.org/10.1149/1945-7111/Abc4c1.

[8] R. Schmuch, R. Wagner, G. Hörpel, T. Placke, M. Winter, Performance and cost of materials for lithium-based rechargeable automotive batteries, Nat. Energy 3 (4) (2018) 267–278, http://dx.doi.org/10.1038/s41560-018-0107-2.

[9] C. Martin, Driving change in the battery industry, Nature Nanotechnol. 9 (5) (2014) 327–328, http://dx.doi.org/10.1038/nnano.2014.92.

[10] M. Greenwood, M. Wentker, J. Leker, A bottom-up performance and cost assessment of lithium-ion battery pouch cells utilizing nickel-rich cathode active materials and silicon-graphite composite anodes, J. Power Sources Adv. 9 (2021) 100055, http://dx.doi.org/10.1016/j.powera.2021.100055.

[11] K. Kalaga, M.-T.F. Rodrigues, S.E. Trask, I.A. Shkrob, D.P. Abraham, Calendar-life versus cycle-life aging of lithium-ion cells with silicon-graphite composite electrodes, Electrochim. Acta 280 (2018) 221–228, http://dx.doi.org/10.1016/j.electacta.2018.05.101.

[12] J.D. McBrayer, M.-T.F. Rodrigues, M.C. Schulze, D.P. Abraham, C.A. Apblett, I. Bloom, G.M. Carroll, A.M. Colclasure, C. Fang, K.L. Harrison, G. Liu, S.D. Minteer, N.R. Neale, G.M. Veith, C.S. Johnson, J.T. Vaughey, A.K. Burrell, B. Cunningham, Calendar aging of silicon-containing batteries, Nature Energy 6 (2021) 866–872, http://dx.doi.org/10.1038/s41560-021-00883-w.

[13] M. Schindler, J. Sturm, S. Ludwig, A. Durdel, A. Jossen, Comprehensive analysis of the aging behavior of nickel-rich, silicon-graphite lithium-ion cells subject to varying temperature and charging profiles, J. Electrochem. Soc. 168 (6) (2021) 060522, http://dx.doi.org/10.1149/1945-7111/ac03f6.

[14] J. Schmitt, M. Schindler, A. Jossen, Change in the half-cell open-circuit potential curves of silicon–graphite and nickel-rich lithium nickel manganese cobalt oxide during cycle aging, J. Power Sources 506 (2021) 230240, http://dx.doi.org/10.1016/j.jpowsour.2021.230240.

[15] S. Ma, M. Jiang, P. Tao, C. Song, J. Wu, J. Wang, T. Deng, W. Shang, Temperature effect and thermal impact in lithium-ion batteries: A review, Prog. Nat. Sci.: Mater. Int. 28 (6) (2018) 653–666, http://dx.doi.org/10.1016/j.pnsc.2018.11.002.

[16] T. Waldmann, M. Wilka, M. Kasper, M. Fleischhammer, M. Wohlfahrt-Mehrens, Temperature dependent ageing mechanisms in lithium-ion batteries – A post-mortem study, J. Power Sources 262 (2014) 129–135, http://dx.doi.org/10.1016/j.jpowsour.2014.03.112.

[17] R.R. Richardson, P.T. Ireland, D.A. Howey, Battery internal temperature estimation by combined impedance and surface temperature measurement, J. Power Sources 265 (2014) 254–261, http://dx.doi.org/10.1016/j.jpowsour.2014.04.129.

[18] R.R. Richardson, D.A. Howey, Sensorless battery internal temperature estimation using a Kalman filter with impedance measurement, IEEE Trans. Sustain. Energy 6 (4) (2015) 1190–1199, http://dx.doi.org/10.1109/TSTE.2015.2420375.

[19] K.M. Carthy, H. Gullapalli, K.M. Ryan, T. Kennedy, Review–use of impedance spectroscopy for the estimation of Li-ion battery state of charge, state of health and internal temperature, J. Electrochem. Soc. 168 (8) (2021) 080517, http://dx.doi.org/10.1149/1945-7111/ac1a85.

[20] H. Beelen, K. Mundaragi Shivakumar, L. Raijmakers, M. Donkers, H.J. Bergveld, Towards impedance-based temperature estimation for Li-ion battery packs, Int. J. Energy Res. 44 (4) (2020) 2889–2908, http://dx.doi.org/10.1002/er.5107.

[21] X. Hu, W. Liu, X. Lin, Y. Xie, A comparative study of control-oriented thermal models for cylindrical Li-ion batteries, IEEE Trans. Transp. Electrification 5 (4) (2019) 1237–1253, http://dx.doi.org/10.1109/TTE.2019.2953606.

[22] S. Ludwig, I. Zilberman, A. Oberbauer, M. Rogge, M. Fischer, M. Rehm, A. Jossen, Adaptive method for sensorless temperature estimation over the lifetime of lithium-ion batteries, J. Power Sources 521 (2022) 230864, http://dx.doi.org/10.1016/j.jpowsour.2021.230864.

[23] S. Ludwig, I. Zilberman, M. Horsche, T. Wohlers, A. Jossen, Pulse resistance based online temperature estimation for lithium-ion cells, J. Power Sources 490 (2021) 229523, http://dx.doi.org/10.1016/j.jpowsour.2021.229523.

[24] Y. Wang, J. Tian, Z. Sun, L. Wang, R. Xu, M. Li, Z. Chen, A comprehensive review of battery modeling and state estimation approaches for advanced battery management systems, Renew. Sustain. Energy Rev. 131 (2020) 110015, http://dx.doi.org/10.1016/j.rser.2020.110015.

[25] A. Fotouhi, D.J. Auger, K. Propp, S. Longo, M. Wild, A review on electric vehicle battery modelling: From lithium-ion toward lithium–sulphur, Renew. Sustain. Energy Rev. 56 (2016) 1008–1021, http://dx.doi.org/10.1016/j.rser.2015.12.009.

[26] D.U.S. Alexander Farmann, Comparative study of reduced order equivalent circuit models for on-board state-of-available-power prediction of lithium-ion batteries in electric vehicles, Appl. Energy 225 (2018) 1102–1122, http://dx.doi.org/10.1016/j.apenergy.2018.05.066.

[27] X. Hu, F. Feng, K. Liu, L. Zhang, J. Xie, B. Liu, State estimation for advanced battery management: Key challenges and future trends, Renew. Sustain. Energy Rev. 114 (2019) 109334, http://dx.doi.org/10.1016/j.rser.2019.109334.

[28] C. Li, N. Cui, Z. Cui, C. Wang, C. Zhang, Novel equivalent circuit model for high-energy lithium-ion batteries considering the effect of nonlinear solid-phase diffusion, J. Power Sources 523 (2022) 230993, http://dx.doi.org/10.1016/j.jpowsour.2022.230993.

[29] D. Chen, L. Xiao, W. Yan, Y. Guo, A novel hybrid equivalent circuit model for lithium-ion battery considering nonlinear capacity effects, Energy Rep. 7 (2021) (2021) http://dx.doi.org/10.1016/j.egyr.2021.06.051, 320–329 6th International Conference on Advances on Clean Energy Research.

[30] A. Chen, W. Zhang, C. Zhang, W. Huang, S. Liu, A temperature and current rate adaptive model for high-power lithium-titanate batteries used in electric vehicles, IEEE Trans. Ind. Electron. 67 (11) (2020) 9492–9502, http://dx.doi.org/10.1109/TIE.2019.2955413.

[31] T. Heil, A. Jossen, Continuous approximation of the ZARC element with passive components, Meas. Sci. Technol. 32 (10) (2021) 104011, http://dx.doi.org/10.1088/1361-6501/ac0466.

[32] X. Hu, H. Yuan, C. Zou, Z. Li, L. Zhang, Co-estimation of state of charge and state of health for lithium-ion batteries based on fractional-order calculus, IEEE Trans. Veh. Technol. 67 (2018) 10319–10329, http://dx.doi.org/10.1109/TVT.2018.2865664.

[33] R. Xiong, J. Tian, W. Shen, F. Sun, A novel fractional order model for state of charge estimation in lithium ion batteries, IEEE Trans. Veh. Technol. 68 (5) (2019) 4130–4139, http://dx.doi.org/10.1109/TVT.2018.2880085.

[34] Z. Chen, Y. Fu, C.C. Mi, State of charge estimation of lithium-ion batteries in electric drive vehicles using extended Kalman filtering, IEEE Trans. Veh. Technol. 62 (3) (2013) 1020–1030, http://dx.doi.org/10.1109/TVT.2012.2235474.

[35] F. Naseri, E. Schaltz, D.-I. Stroe, A. Gismero, E. Farjah, An enhanced equivalent circuit model with real-time parameter identification for battery state-of-charge estimation, IEEE Trans. Ind. Electron. 69 (4) (2022) 3743–3751, http://dx.doi.org/10.1109/TIE.2021.3071679.

[36] P. Shrivastava, T. Kok Soon, M.Y.I. Bin Idris, S. Mekhilef, S.B.R.S. Adnan, Combined state of charge and state of energy estimation of lithium-ion battery using dual forgetting factor-based adaptive extended Kalman filter for electric vehicle applications, IEEE Trans. Veh. Technol. 70 (2) (2021) 1200–1215, http://dx.doi.org/10.1109/TVT.2021.3051655.

[37] F. An, J. Jiang, W. Zhang, C. Zhang, X. Fan, State of energy estimation for lithium-ion battery pack via prediction in electric vehicle applications, IEEE Trans. Veh. Technol. 71 (1) (2022) 184–195, http://dx.doi.org/10.1109/TVT.2021.3125194.

[38] Q. Yu, R. Xiong, C. Lin, W. Shen, J. Deng, Lithium-ion battery parameters and state-of-charge joint estimation based on H-infinity and unscented Kalman filters, IEEE Trans. Veh. Technol. 66 (10) (2017) 8693–8701, http://dx.doi.org/10.1109/TVT.2017.2709326.

[39] Z. He, Z. Yang, X. Cui, E. Li, A method of state-of-charge estimation for EV power lithium-ion battery using a novel adaptive extended Kalman filter, IEEE Trans. Veh. Technol. 69 (12) (2020) 14618–14630, http://dx.doi.org/10.1109/TVT.2020.3032201.

[40] S. Nejad, D. Gladwin, D. Stone, A systematic review of lumped-parameter equivalent circuit models for real-time estimation of lithium-ion battery states, J. Power Sources 316 (2016) 183–196, http://dx.doi.org/10.1016/j.jpowsour.2016.03.042.

[41] N. Wassiliadis, J. Adermann, A. Frericks, M. Pak, C. Reiter, B. Lohmann, M. Lienkamp, Revisiting the dual extended Kalman filter for battery state-of-charge and state-of-health estimation: A use-case life cycle analysis, J. Energy Storage 19 (2018) 73–87, http://dx.doi.org/10.1016/j.est.2018.07.006.

[42] J. Park, M. Lee, G. Kim, S. Park, J. Kim, Integrated approach based on dual extended Kalman filter and multivariate autoregressive model for predicting battery capacity using health indicator and SOC/SOH, Energies 13 (9) (2020) http://dx.doi.org/10.3390/en13092138.

[43] W. Yan, B. Zhang, G. Zhao, S. Tang, G. Niu, X. Wang, A battery management system with a Lebesgue-sampling-based extended Kalman filter, IEEE Trans. Ind. Electron. 66 (4) (2019) 3227–3236, http://dx.doi.org/10.1109/TIE.2018.2842782.

[44] M. Schimpe, M.E. von Kuepach, M. Naumann, H.C. Hesse, K. Smith, A. Jossen, Comprehensive modeling of temperature-dependent degradation mechanisms in lithium iron phosphate batteries, J. Electrochem. Soc. 165 (2) (2018) A181–A193, http://dx.doi.org/10.1149/2.1181714jes.

[45] J. Schmalstieg, S. Käbitz, M. Ecker, D.U. Sauer, A holistic aging model for Li(NiMnCo)O2 based 18650 lithium-ion batteries, J. Power Sources 257 (2014) 325–334, http://dx.doi.org/10.1016/j.jpowsour.2014.02.012.

[46] J. Wang, J. Purewal, P. Liu, J. Hicks-Garner, S. Soukazian, E. Sherman, A. Sorenson, L. Vu, H. Tataria, M.W. Verbrugge, Degradation of lithium ion batteries employing graphite negatives and nickel–cobalt–manganese oxide + spinel manganese oxide positives: Part 1, aging mechanisms and life estimation, J. Power Sources 269 (2014) 937–948, http://dx.doi.org/10.1016/j.jpowsour.2014.07.030.

[47] L. Vichard, A. Ravey, P. Venet, F. Harel, S. Pelissier, D. Hissel, A method to estimate battery SOH indicators based on vehicle operating data only, Energy 225 (2021) 120235, http://dx.doi.org/10.1016/j.energy.2021.120235.

[48] P. Shen, M. Ouyang, L. Lu, J. Li, X. Feng, The co-estimation of state of charge, state of health, and state of function for lithium-ion batteries in electric vehicles, IEEE Trans. Veh. Technol. 67 (1) (2018) 92–103, http://dx.doi.org/10.1109/TVT.2017.2751613.

[49] M. Dubarry, G. Baure, Perspective on commercial Li-ion battery testing, best practices for simple and effective protocols, Electronics 9 (1) (2020) http://dx.doi.org/10.3390/electronics9010152.

[50] A. Barai, K. Uddin, M. Dubarry, L. Somerville, A. McGordon, P. Jennings, I. Bloom, A comparison of methodologies for the non-invasive characterisation of commercial Li-ion cells, Prog. Energy Combust. Sci. 72 (2019) 1–31, http://dx.doi.org/10.1016/j.pecs.2019.01.001.

[51] D. Ansean, M. Gonzalez, J.C. Viera, V.M. Garcia, J.C. Alvarez, C. Blanco, Electric vehicle Li-ion battery evaluation based on internal resistance analysis, in: 2014 IEEE Vehicle Power and Propulsion Conference, VPPC, 2014, pp. 1–6, http://dx.doi.org/10.1109/VPPC.2014.7007058.

[52] A. Barai, K. Uddin, W.D. Widanage, A. McGordon, P. Jennings, A study of the influence of measurement timescale on internal resistance characterisation methodologies for lithium-ion cells, Sci. Rep. 8 (1) (2018) 1–13, http://dx.doi.org/10.1038/s41598-017-18424-5.

[53] A. Jossen, Fundamentals of battery dynamics, J. Power Sources 154 (2) (2006) 530–538, http://dx.doi.org/10.1016/j.jpowsour.2005.10.041, selected papers from the Ninth Ulm Electrochemical Days.

[54] A. Farmann, W. Waag, D.U. Sauer, Application-specific electrical characterization of high power batteries with lithium titanate anodes for electric vehicles, Energy 112 (2016) 294–306, http://dx.doi.org/10.1016/j.energy.2016.06.088.

[55] G.L. Plett, Recursive approximate weighted total least squares estimation of battery cell total capacity, J. Power Sources 196 (4) (2011) 2319–2331, http://dx.doi.org/10.1016/j.jpowsour.2010.09.048.

[56] H. Dai, L. Zhu, J. Zhu, X. Wei, Z. Sun, Adaptive Kalman filtering based internal temperature estimation with an equivalent electrical network thermal model for hard-cased batteries, J. Power Sources 293 (2015) 351–365, http://dx.doi.org/10.1016/j.jpowsour.2015.05.087.

[57] Y. Kim, J.B. Siegel, A.G. Stefanopoulou, A computationally efficient thermal model of cylindrical battery cells for the estimation of radially distributed temperatures, in: 2013 American Control Conference, 2013, pp. 698–703, http://dx.doi.org/10.1109/ACC.2013.6579917.

[58] H. Pang, L. Guo, L. Wu, J. Jin, F. Zhang, K. Liu, A novel extended Kalman filter-based battery internal and surface temperature estimation based on an improved electro-thermal model, J. Energy Storage 41 (2021) 102854, http://dx.doi.org/10.1016/j.est.2021.102854.

[59] G. Liu, M. Ouyang, L. Lu, J. Li, X. Han, Analysis of the heat generation of lithium-ion battery during charging and discharging considering different influencing factors, J. Therm. Anal. Calorim. 116 (2) (2014) 1001–1010, http://dx.doi.org/10.1007/s10973-013-3599-9.

[60] S. Huang, X. Wu, G.M. Cavalheiro, X. Du, B. Liu, Z. Du, G. Zhang, In situ measurement of lithium-ion cell internal temperatures during extreme fast charging, J. Electrochem. Soc. 166 (14) (2019) A3254–A3259, http://dx.doi.org/10.1149/2.0441914jes.

[61] L. Chen, M. Hu, K. Cao, S. Li, Z. Su, G. Jin, C. Fu, Core temperature estimation based on electro-thermal model of lithium-ion batteries, Int. J. Energy Res. 44 (7) (2020) 5320–5333, http://dx.doi.org/10.1002/er.5281, URL https://onlinelibrary.wiley.com/doi/abs/10.1002/er.5281.

[62] L. Sheng, Z. Zhang, L. Su, H. Zhang, H. Zhang, Y. Fang, K. Li, W. Ye, Quasi steady state method to measure thermophysical parameters of cylindrical lithium ion batteries, J. Power Sources 485 (2021) 229342, http://dx.doi.org/10.1016/j.jpowsour.2020.229342, URL https://www.sciencedirect.com/science/article/pii/S037877532031630X.

[63] N. Meddings, M. Heinrich, F. Overney, J.S. Lee, V. Ruiz, E. Napolitano, S. Seitz, G. Hinds, R. Raccichini, M. Gaberšček, J. Park, Application of electrochemical impedance spectroscopy to commercial Li-ion cells: A review, J. Power Sources 480 (May) (2020) http://dx.doi.org/10.1016/j.jpowsour.2020.228742.